JOURNAL OF GEOPHYSICAL RESEARCH: OCEANS, VOL. 118, 4542–4552, doi:10.1002/jgrc.20334, 2013

# Wave breaking in developing and mature seas

Johannes Gemmrich,[1] Christopher J. Zappa,[2] Michael L. Banner,[3] and Russel P. Morison[3]

Received 28 May 2013; revised 31 July 2013; accepted 3 August 2013; published 13 September 2013.

[1] In response to the growing need for robust validation data for Phillips (1985) breaking wave spectral framework, we contribute new field results observed from R/P *FLIP* for the breaking crest length distributions, $\Lambda$, during two different wind-wave conditions, and breaking strength during one wind-wave condition. The first experiment in Santa Barbara Channel had developing seas and the second experiment in the central Pacific Ocean south of Hawaii had mature seas. These are among the first experiments to use dissipation rate measurements probing up into the breaking crest together with simultaneous measurements of breaking crest length distributions. We directly measured the effective breaking strength parameter to be $4.2(\pm 1.8) \times 10^{-5}$ in mature seas with wave age, $c_p/u_*$, of 40–47. We also found that the velocity scale of the breaking dissipation rate peak decreases with increasing wave age. Further, the breaking crest length spectrum falls off slower than the $c^{-6}$ behavior predicted by Phillips (1985). The integrated dissipation rate was consistently higher for mature seas compared to developing seas due to higher energy and momentum fluxes from the wind.

**Citation:** Gemmrich, J., C. J. Zappa, M. L. Banner, and R. P. Morison (2013), Wave breaking in developing and mature seas, *J. Geophys. Res. Oceans*, *118*, 4542–4552, doi:10.1002/jgrc.20334.

## 1. Introduction

[2] The breaking of surface waves plays an important role in many air-sea exchange and upper ocean processes, such as the momentum transfer from wind to ocean currents, the transfer of heat and gases from the atmosphere to the ocean surface layer, as well as aerosol generation and increased latent heat flux due to sea spray, to name a few. Wave breaking is the limiting factor in wave growth via dissipation of wave energy, and thus wave breaking is a source of enhanced turbulence kinetic energy in the near-surface layer. In addition, the generation of bubbles associated with the wave-breaking process has strong implications on the optical [*Dickey et al.*, 2011, 2012] and acoustical properties of the upper ocean [*Vagle et al.*, 2012]. Overviews of the role of wave-induced turbulence in upper-ocean dynamics and air-sea exchange processes are given by *Massel* [2009] and *Babanin* [2011].

[3] Despite its importance and wide spread occurrence, wave breaking is still difficult to quantify in the field [*Babanin*, 2011; *Perlin et al.*, 2013]. A promising approach is a spectral framework for breaking waves and their dynamics proposed by *Phillips* [1985]. In this context, the key measure for quantifying wave breaking is the spectral density of breaking crest length per unit area, $\Lambda(c_b, \theta)$, where $c_b$ and $\theta$ are the breaker crest speed and crest propagation direction, respectively. Several recent studies were conducted to remotely sense these parameters in the field, using hydrophone arrays [*Ding and Farmer*, 1994], HF-Radar [*Phillips et al.*, 2001], and video imagery [*Melville and Matusov*, 2002; *Gemmrich et al.*, 2008; *Mironov and Dulov*, 2008; *Thomson et al.*, 2009; *Kleiss and Melville*, 2010], although not all of these studies provided the full set of parameters to estimate $\Lambda(c_b, \theta)$.

[4] Various moments of $\Lambda(c_b, \theta)$ can be used to estimate a number of key air-sea interfacial properties, including the mean total length of breaking crests per unit area

$$L = \int \Lambda(c_b, \theta) c_b \mathrm{d}c_b \mathrm{d}\theta, \tag{1}$$

the rate of surface overturning, which is equivalent to the rate of breaking waves moving past a fixed point,

$$R = \int c_b \Lambda(c_b, \theta) c_b \mathrm{d}c_b \mathrm{d}\theta, \tag{2}$$

the momentum flux from waves to currents

$$M = b_{\mathrm{eff}}\, \rho g^{-1} \int c_b^4 \Lambda(c_b, \theta) c_b \mathrm{d}c_b \mathrm{d}\theta, \tag{3}$$

the upper ocean dissipation rate due to wave breaking at a specific scale

[1]Department of Physics and Astronomy, University of Victoria, Victoria, British Columbia, Canada.
[2]Ocean and Climate Physics Division, Lamont-Doherty Earth Observatory of Columbia University, Palisades, New York, USA.
[3]School of Mathematics and Statistics, University of New South Wales, Sydney, New South Wales, Australia.

Corresponding author: J. Gemmrich, Department of Physics and Astronomy, University of Victoria, PO Box 3055, Victoria, BC V8W 3P6, Canada. (gemmrich@uvic.ca)


2169-9275/13/10.1002/jgrc.20334

$$\varepsilon(c_b) = b(c_b)\rho g^{-1} c_b^5 \Lambda(c_b), \tag{4}$$

where

$$\Lambda(c_b) = \int \Lambda(c_b, \theta) c_b \mathrm{d}\theta, \tag{5}$$

and the total dissipation rate due to wave breaking

$$E = b_{\mathrm{eff}}\, \rho g^{-1} \int c_b^5 \Lambda(c_b, \theta) c_b \mathrm{d}c_b \mathrm{d}\theta, \tag{6}$$

where $g$ is the gravitational acceleration, $\rho$ is the density of sea water, and $b_{\mathrm{eff}}$ is a nondimensional factor. We call $b_{\mathrm{eff}}$ the *effective breaking strength parameter*, and it represents a weighted average of the spectrally resolved, but so far unknown $b(c_b)$.

[5] Laboratory studies have shown that breaking crests travel measurably more slowly than the corresponding unbroken waves from which they evolve [e.g., *Rapp and Melville*, 1990; *Stansell and MacFarlane*, 2002], and it was proposed that $c_b = \alpha c$, where $\alpha$ was estimated to lie in the range 0.7–0.9 in these laboratory studies of idealized 2-D wave packets. Notwithstanding this complication, the $\Lambda(c_b, \theta)$ distribution is emerging as a useful spectral description of wave-breaking kinematics, and has potential extension to wave-breaking dynamics. Here we analyze the variability of breaking crest length distributions based on data obtained at two contrasting ocean sites, and their relation to near-surface turbulence for one data set.

## 2. Observations

[6] The two experiments were conducted from aboard R/P *FLIP* and took place in September 2008 in the Santa Barbara Channel (SBC) and in September 2009 south of the Hawaiian Islands (HI). As part of the RaDyO field program [*Dickey et al*., 2012], we obtained a suite of wave field observations, turbulence measurements, and air-sea fluxes. Details on the instrumentation and environmental conditions are given in *Zappa et al*. [2012]. In particular, data from two scanning lidars and a sonic anemometer mounted on the starboard boom of R/P *FLIP* yielded significant wave height $H_s$ and atmospheric friction velocity $u_*$, respectively. Relevant time series of $H_s$ and $u_*$ are shown in Figures 7a and 7c.

[7] Here we focus on video imagery obtained from two digital video cameras with 1024 × 1360 resolution, 12 bit digitization depth, and 20 Hz frame rate. These cameras were used to observe wave breaking and whitecaps. A small field of view camera was mounted on R/P *FLIP*'s starboard boom, resulting in a field of view of roughly 10 m by 15 m. A second camera was deployed from the crow's nest at 26 m above sea level, yielding a field of view of roughly 100 m by 200 m to record larger-scale breaking events. These two cameras were recording simultaneously, usually for 30 min of each hour if the light conditions were favorable.

[8] Overall, 37 h of data were recorded during the SBC experiment on 14–23 September 2008 and 20 h of data were recorded during the experiment off Hawaii on 4–11 September 2009.

[9] In situ observations of the near-surface turbulence field were obtained during the Hawaii experiment with a set of three 2 MHz single beam Doppler sonars (Dopbeam, Sontek) mounted on a surface float tethered between the starboard and center booms of R/P *FLIP* [*Vagle et al*., 2012].

[10] The Dopbeams acquired radial velocity with high spatial ($6 \times 10^{-3}$m) and temporal (20 Hz) resolution, along a profile from the free surface to 0.7 m and from 1.04 m to 1.75 m depths. Profiles of turbulence kinetic energy dissipation rate $\varepsilon(z,t)$ are estimated from the velocity profiles, based on centered second-order structure functions [*Gemmrich*, 2010; *Vagle et al*., 2012]. The dissipation rate profiles are integrated in space and averaged over several minutes to obtain a robust estimate of the total energy dissipation rate in the upper water column:

$$E_{dis} = \left\langle \int_{z_2}^{0} \varepsilon(z,t)\mathrm{d}z \right\rangle \tag{7}$$

where $z_2 = -1.75$m and $< >$ represents the mean over 500 s.

## 3. Breaking Crest Speed

[11] Following the *Phillips* [1985] framework, the scale of a breaking wave is ideally specified by its wave number, which can be difficult to measure in the field. Phillips proposed using the breaker velocity as a surrogate, where he assumed the breaker velocity matches the phase velocity of the underlying wave that is breaking. The deep water dispersion relation then allows transforming measured breaking crest length spectral distributions observed as a function of breaker velocity to the wavenumber domain via the dispersion relation. However, ocean breaking waves are unsteady and the speed of a breaking crest slows down with time [*Gemmrich et al*., 2008; *Kleiss and Melville*, 2011]. Thus, the spatial scale of the wave can only be determined accurately from the *initial* breaker velocity and not from the time-varying breaker velocity. Furthermore, due to a crest slowdown effect associated with wave group bandwidth and nonlinearity, the equivalent linear phase speed $c$ is slightly higher than the propagation speed $c_b$ of the breaking crest, $c = \alpha^{-1} c_b$. The exact value of the scaling factor $\alpha$ is not known as yet, although it is generally taken in the range $0.7 < \alpha < 0.9$ [*Gemmrich et al*., 2008]. Therefore, we present the following analysis in terms of $c_b$. Pending future determination of $\alpha$, our results can then be converted into true phase velocities and then into the wavenumber domain.

## 4. Methodology

[12] Our automated analysis of the video imagery extracts the propagation speed $c_b$, the propagation direction $\theta$, and the length of the breaking segments $L$ for each individual breaking event. The extraction of these breaking crest parameters follows the methodology described in detail in *Gemmrich et al*. [2008], and is briefly summarized here. The breaking crest length is extracted from binary images generated from the difference between successive

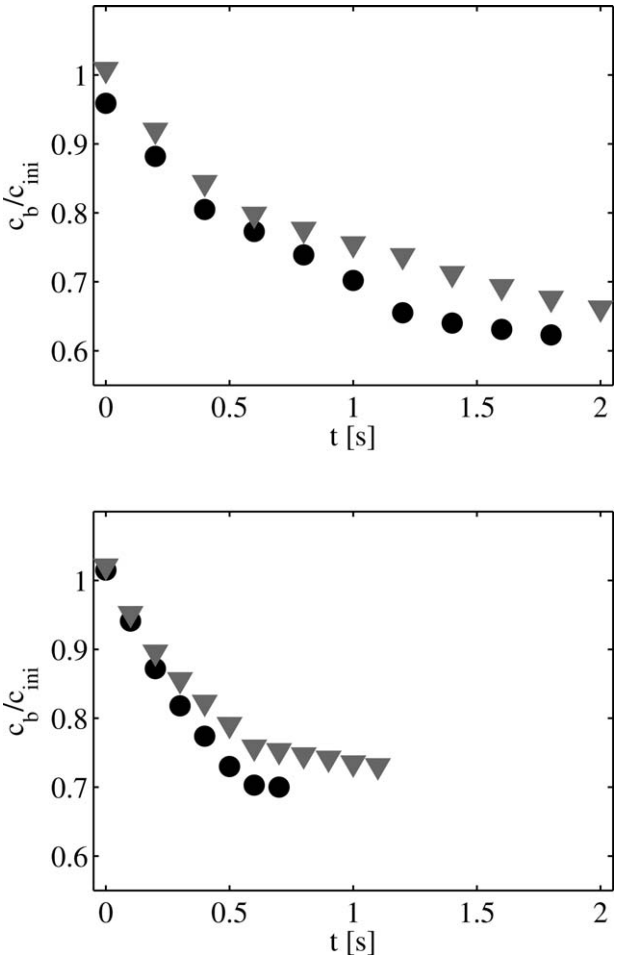


**Figure 1.** Average temporal evolution of normalized crest propagation speeds. For (top) Santa Barbara Channel and (bottom) Hawaii, obtained from the small view camera (black circles) and the large field of view camera (gray triangles).

images. In these differential images, the forward edge of a breaking crest results in a strong positive signal, and stationary features as well as the bulk of a whitecap are eliminated.

[13] Next, each breaking crest is treated as an image object and its centroid location, major and minor axis length, and orientation are recorded onto a file. Occasionally, the thresholding mechanism splits a single whitecap edge into several objects. Neighboring objects with similar orientation and propagation properties are combined into single objects. However, treating these segments as individual breaking events will result in the same breaking crest length distribution as processing the recombined objects.

[14] Tracking the location of the object centroid across subsequent images provides the propagation speed and orientation of breaking crests. Generally, the observed speed is highest at the beginning of a breaking event. The average evolution of the propagation speed is given in Figure 1 where $c_b$ is normalized by the initial speed $c_{ini}$ of a particular event. Speed values fluctuate during the evolution of the event, most likely due to measurement uncertainties, so that the initial speed does not always collapse with the first data point. To smooth out these fluctuations, we calculate a least squares linear fit of the first half of the velocity estimates and evaluate it at $t = 0$. This calculated initial speed is then assigned to be the characteristic breaking crest speed $c_b$ of an individual event. The speed of breaking crests that originate upstream from the camera field of view and propagate into the image will necessarily be underestimated. However, for the large field of view camera, these events contribute only a small fraction of the total number of events and the introduced error in the speed distribution is small.

[15] For long waves, the whitecap displacement velocity represents the true whitecap propagation, i.e., the nonlinear phase velocity of the breaking wave [*Gemmrich et al.*, 2008]. The whitecap displacement velocity can be modified by advection, where the advection velocity $\mathbf{v}_{adv} = \mathbf{v}_{orb} + \mathbf{U}$ is a combination of surface currents $\mathbf{U}$ and the orbital motion $|v_{orb}| \approx a\omega$, of underlying longer waves with long wave amplitude $a$ and frequency $\omega$ [*Gemmrich et al.*, 2008]. Breaking crests of shorter waves riding on longer waves will be advected by the orbital motion of underlying long waves. Typically, the maximum orbital advection speeds are $0.9\,\mathrm{ms}^{-1}$ for the Santa Barbara Channel experiment and $1.2\,\mathrm{ms}^{-1}$ for the Hawaii data set. The maximum advection due to orbital motions occurs at the crest of the long wave and only if the propagation direction of long waves and breaking short waves are aligned [*Gemmrich et al.*, 2008]. Surface currents in SBC were $U = 0.23\ (\pm 0.09)\,\mathrm{ms}^{-1}$, propagating toward $113^{\circ} \pm 50^{\circ}$. During HI, based on visual observations, surface currents relative to the drifting R/P *FLIP* were weaker than in SBC. While short wave breaking events often occur near the crest of the longer waves, their propagation directions are not necessarily aligned. Thus, on average $|v_{adv}| < 1\,\mathrm{ms}^{-1}$ for short waves, and $|v_{adv}| \ll 1\,\mathrm{ms}^{-1}$ for waves at intermediate scales [*Gemmrich et al.*, 2008].

[16] The breaking crest length distributions $\Lambda(c_b)$ for a given speed range $(c_b, c_b + \Delta c_b)$ are calculated, following *Gemmrich et al.* [2008], as the summation of breaking crest length segments over all events, normalized by the total area of the field of view $A$ and the total observation time $T$

$$\Lambda(c_b) = \sum L_{br} t_{br} / (TA\Delta c_b) \tag{8}$$

where $t_{br}$ and $L_{br}$ are the duration and characteristic breaking segment length of individual events, respectively. The length of a breaking crest is evolving during the active breaking period, first increasing and then decreasing [*Kleiss and Melville*, 2011], and we take the mean value over $t_{br}$ as the representative length scale $L_{br}$ for that breaking event. Note, *Gemmrich et al.* [2008] used the maximum length of individual breaking segments, which yields $\approx$30% overestimation of $\Lambda(c_b)$, when compared to the values reported here.

## 5. Properties of Breaking Crest Lengths

[17] The distributions of the breaking crest parameters (propagation speed $c_b$, the propagation direction $\theta$, and the length of the breaking segments $L$) depend on the wave field and are given in Figure 2. Generally, the distributions

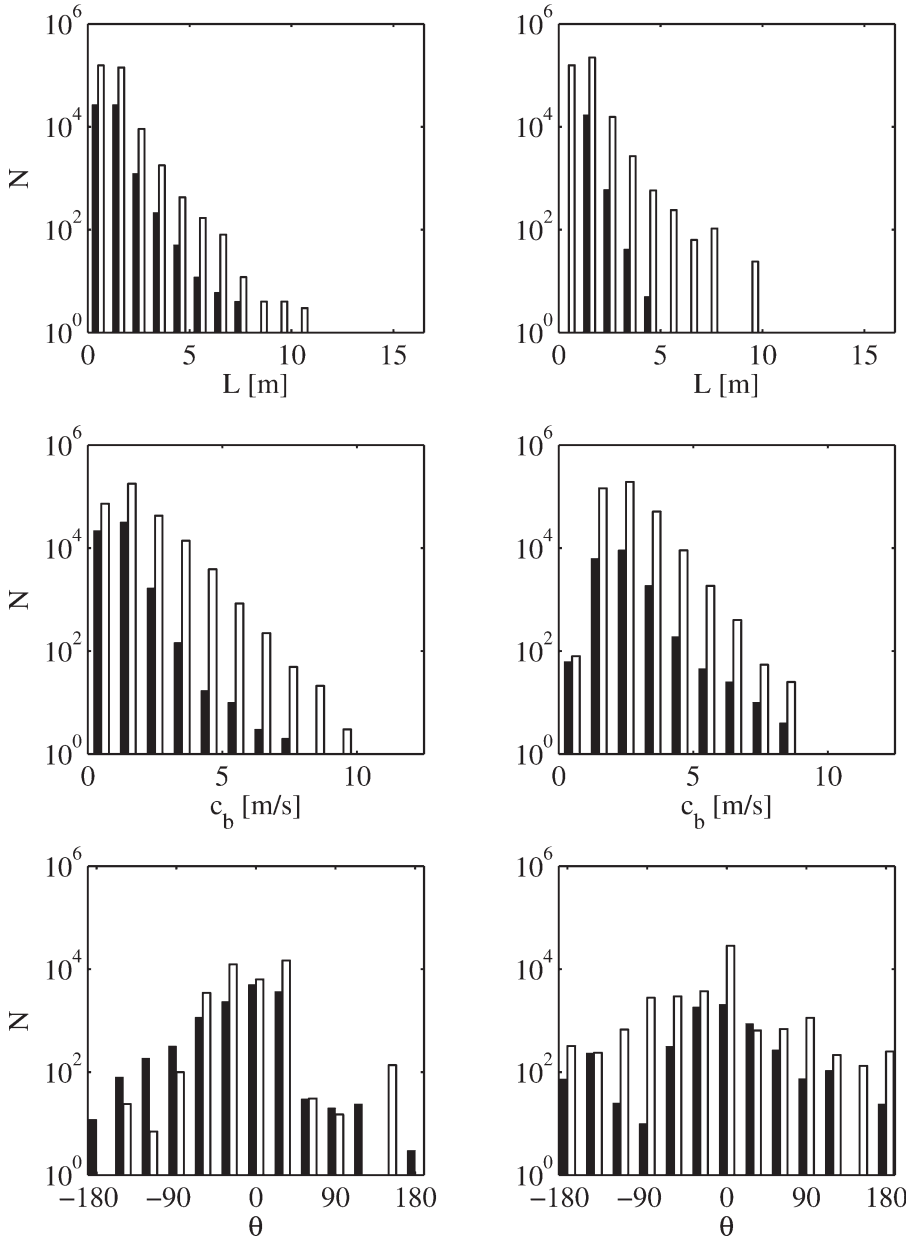


**Figure 2.** Histogram of properties of breaking crest segments: (top) length L, (middle) propagation speed $c_b$, and (bottom) propagation direction $\theta$. (left) Data for SBC and (right) data for HI, obtained from the small view camera (black bars) and the large field of view camera (white bars). (Note logarithmic scale. Total data acquisition time in SBC is almost twice as long as in HI).

obtained from the small field of view (FOV) camera data are in good agreement with the distributions obtained from the larger FOV camera data. However, the distributions of speed and length clearly show the cutoff of larger values inherent in the spatial limits of the small field of view.

[18] The most commonly observed length of breaking crest segments is in the $1-2$ m range for both the SBC and HI data sets. The maximum length is more than 15 m in the Santa Barbara Channel, but significantly less off Hawaii. Visual observations from aboard R/P *FLIP* as well as ENVISAT SAR images (20 September 2008) indicate two roughly unidirectional wave systems at $\approx 120^{\circ}$ to each other dominated the wave field at the experimental site in SBC: wind waves approaching from the west and southerly swell, being refracted by the islands to propagate toward NNW. This resulted in fairly long-crested waves and is reflected in the length distribution of the breaking crest segments and the asymmetric distribution of breaking crest propagation directions $\theta$. During the Hawaii experiment, the wave field had a broad directional distribution, and the resulting short-crestedness can be seen in the reduced number of long breaking segments and the symmetric and somewhat flatter $\theta$ distribution.

## 6. Breaking Crest Length Distributions

[19] Results on the breaking crest length distribution $\Lambda(c_b)$ for the two experiments are given in Figure 3. A key

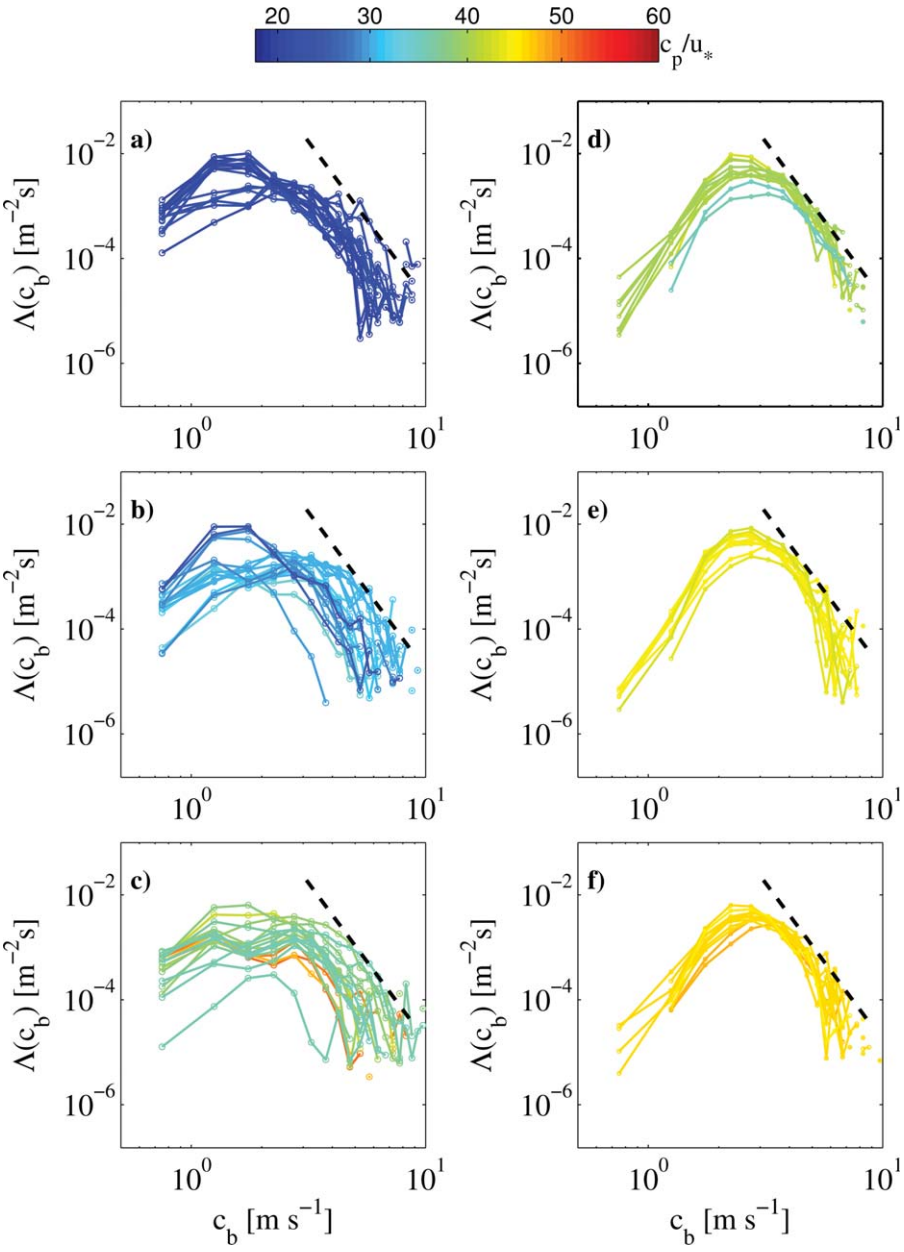


**Figure 3.** Breaking crest length distributions during the experiments in (a–c) Santa Barbara Channel and(d–f) Hawaii. Colors represent wave age $c_p/u_*$. The dashed line indicates the $m = -6$ slope predicted by *Phillips* [1985]. For each experiment, data runs are split into three equal-sized subpanels, covering the entire data sets.

feature of all observed $\Lambda(c_b)$ distributions at both experimental sites is a maximum at short-to-intermediate wave scales. The location of this maximum, which specifies the scale of the largest contribution of breaking crests, increases with wave age; however, there is no clear dependence on wave age of the magnitude of this maximum.

[20] Wind speed and wave field parameters covered a much broader range during the Santa Barbara Channel experiment compared to the experiment in the central Pacific Ocean south of Hawaii. These differences in the dynamic range of forcing parameters are directly reflected in the dynamic range of the breaking crest length distributions. At intermediate scales, i.e., $3\,\mathrm{m/s} \leq c_b \leq 5\mathrm{m/s}$, the $\Lambda$-distributions span almost 2 orders of magnitude in SBC, but only a factor ≈5 in HI. The maximum levels of $\Lambda(c_b)$ are comparable between the two experiments, but the overall mean level of $\Lambda(c_b)$ is larger in HI. The exponent of the $\Lambda(c_b)$ curves for higher $c_b$ values fluctuates about the *Phillips* [1985] canonical form $\Lambda(c_b) \propto c_b^{-6}$, which will be discussed in detail below.

[21] The normalized fifth moment of the breaking crest length distributions is given in Figure 4. The fifth moment of the $\Lambda(c_b)$ distribution is related to the spectral energy dissipation rate $\varepsilon(c_b)$ given in equation (4). However, the transition from the kinematic quantity of the crest length distribution to the dynamics of energy

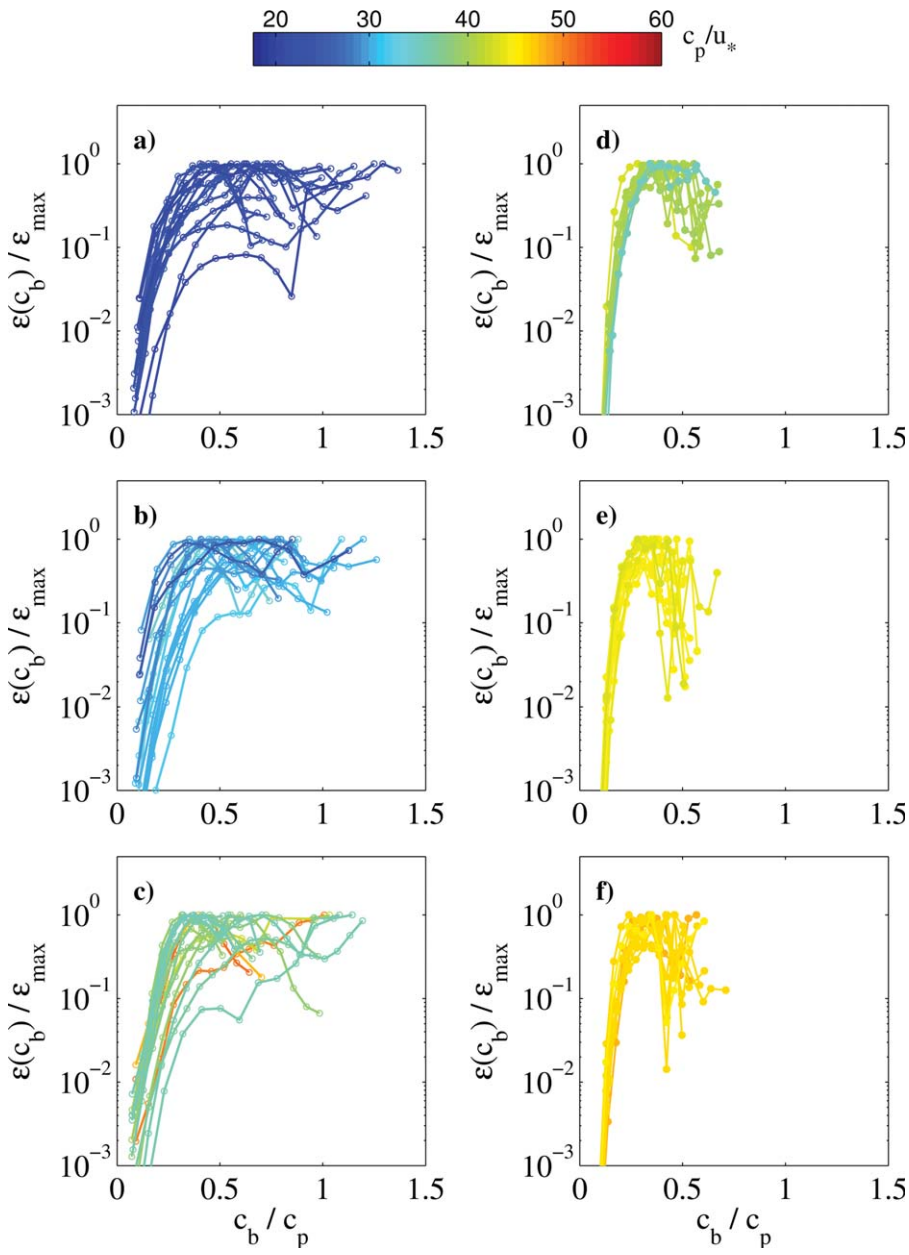


**Figure 4.** Normalized fifth moment of breaking crest length distributions, representing spectral energy dissipation rate $\epsilon/\epsilon_{max}$ for the experiments in (a–c) Santa Barbara Channel and (d–f) Hawaii. Colours indicate wave age $c_p/u_*$. For each experiment, data runs are split into three equal-sized subpanels, covering the entire data sets.

dissipation rate requires knowledge of the breaking strength parameter $b(c_b)$. Estimates of the spectrally resolved breaking strength parameter are only starting to become available and all previous studies based on field data report the scale-integrated value $b_{\text{eff}}$. Reported values of $b_{\text{eff}}$ from different experiments span more than 3 orders of magnitude between these experiments, from $3 \times 10^{-5}$ to $7 \times 10^{-2}$ [*Melville and Matusov*, 2002; *Gemmrich et al.*, 2008; *Thomson et al.*, 2009]. Note, the $\Lambda$-distributions given in *Melville and Matusov* [2002] yield unrealistically low breaking rates and therefore the value $b_{\text{eff}} = 7 \times 10^{-2}$ is likely too high. Recent work by *Romero et al.* [2012] suggests that approximating $b(c_b)$ by a uniform level, independent of $c_b$, is a reasonable approach, at least for wave scales shorter than the dominant waves.

[22] The relative importance of energy dissipation rate across the wave spectrum is

$$\varepsilon_{norm}(c_b) = \frac{b(c_b)c_b^5\Lambda(c_b)}{max\left[b(c_b)c_b^5\Lambda(c_b)\right]} \tag{9}$$

[23] Thus, for the approximation that $b$ is only a function of the environmental conditions and is nearly independent of the wave scale, Figure 4 represents the relative

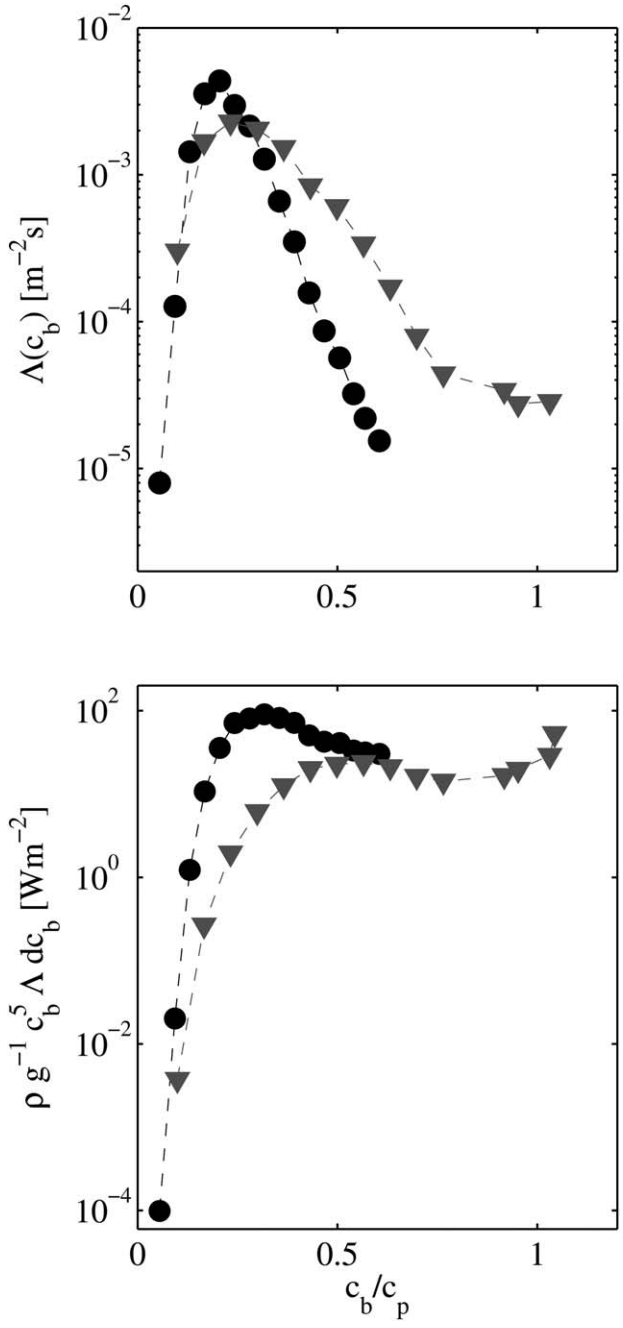


**Figure 5.** (top) Average breaking crest length distributions and (bottom) their fifth moment, for subsets of the data representing developing seas (gray triangles) and mature seas (black circles).

importance of energy dissipation rate across the wave spectrum $\varepsilon(c_b)/\varepsilon_{max}$.

[24] There are some noteworthy differences in the shape of breaking crest length distributions of the two data sets, likely associated with different development stages of the wave field. We calculate average distributions from 24 SBC runs with $c_p/u_* \leq 25$, characterizing growing seas, and from 14 HI runs with $c_p/u_* \geq 45$, characterizing mature seas (Figure 5). There were no comparably mature sea states from the SBC data set to include. In growing seas, breaking spans the entire spectrum from dominant waves to scales associated with $0.1c_p$, whereas in mature seas no breaking is observed at scales larger than those corresponding to $0.6c_p$. Similarly, the strongest dissipation rate occurs at small-to-intermediate scales in the mature seas, but at the large wave scale in the developing seas. Despite the fact that breaking in mature seas is concentrated over a smaller spectral band than in growing seas, the total dissipation rate in the mature seas is about 3 times higher.

[25] Interestingly, the momentum flux $\tau = \rho_{air} u_*^2$ in the air surface boundary layer, where $\rho_{air}$ is the density of air, is also 3 times higher in HI compared to SBC. Since the energy input into the wave field $E_{in} = c_{\mathrm{eff}}\, \tau$, where $c_{\mathrm{eff}}$ is an effective phase speed [*Gemmrich et al.*, 1994], nearly balances the energy dissipation, we conclude that the effective phase speed $c_{\mathrm{eff}}$ does not vary significantly between the two experimental conditions.

[26] The overview of all individual runs indicates the dominant scale of energy dissipation shifting toward smaller scales as the wave field develops (Figure 4). Indeed, a more detailed analysis of the dominant scale of the energy dissipation $\Gamma_p = c_b(\varepsilon_{max})/c_p$ confirms this behavior (Figure 6). In young seas the strongest dissipation rate occurs close to the scale of the dominant waves. However, in more developed seas the energy dissipation rate peaks at short-to-intermediate scales, with rapid decrease toward shorter and longer waves. The combined SBC and HI data show the trend of decreasing dominant dissipation scale $\Gamma_p$ with increasing wave age, unlike the total dissipation rate.

[27] The breaking rate $R$ is a purely kinematic quantity given by the first moment of $\Lambda(c_b)$ (equation (2)). In both

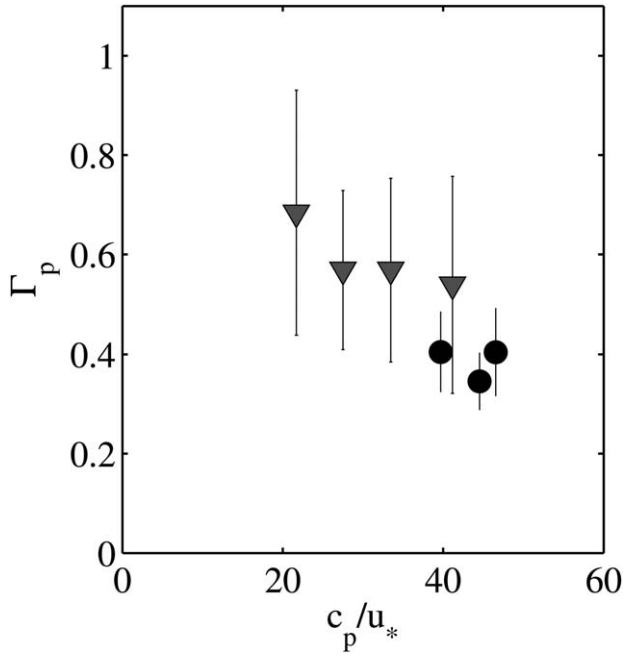


**Figure 6.** Bin-averaged peak of the fifth moment of breaking crest length distributions, in terms of the normalized velocity $\Gamma_p$, as function of wave age $c_p/u_*$ for the Santa Barbara Channel (gray triangles) and Hawaii experiment (black circles).

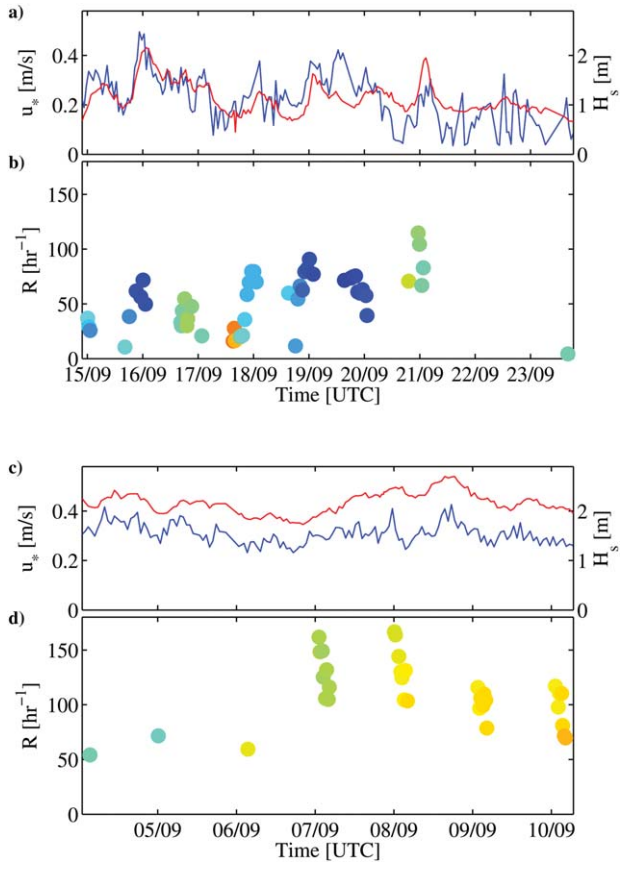


**Figure 7.** Significant wave height $H_s$ (red), friction velocity $u_*$ (blue), and breaking rate $R$ (first moment of breaking crest length distributions) for (a, b) Santa Barbara Channel and (c, d) Hawaii experiment. Colour coding of breaking rates depicts wave age (same scale as in Figure 3).

experiments the breaking rate follows the fluctuations of the wind forcing on individual days, i.e., the setup of a land-sea breeze system with strongly increasing winds during the day in SBC, and slightly decreasing wind speeds in the afternoon in HI [*Zappa et al.*, 2012]. In SBC, the breaking rate increased from $R \approx 15\text{h}^{-1}$ to $R \approx 80 - 100\text{h}^{-1}$ (Figure 7a). In HI, breaking rates were generally higher, up to $R \approx 150\text{h}^{-1}$ in the late morning, decreasing to $R \approx 100\text{h}^{-1}$ in the late afternoon (Figure 7b). For individual records within a given day in HI, as well as for the daily average, the breaking rate is inversely correlated with wave age. However, on different days, similar wave age values can be associated with breaking rates differing by 50% or more. Similarly, while there is a general tendency of higher breaking rates during conditions of stronger wind forcing, the breaking rate clearly cannot be derived from wind speed alone.

## 7. Discussion

[28] As a first approximation $E/b_{\text{eff}}$, the total dissipation rate, $E$, scaled by the effective breaking strength parameter, $b_{\text{eff}}$ (i.e., integrated fifth moment of $\Lambda$) increases roughly linearly with the breaking rate $R$ (Figure 8). In particular, for conditions of infrequent breaking, $R < 50\text{h}^{-1}$, the relation between dissipation rate and breaking rate is rather close. These cases represent mainly older sea states in SBC, where the energy dissipation rate is concentrated in a narrow spectral band at scales much smaller than the dominant waves (Figure 4c). However, the highest breaking rates in SBC, $R \approx 50 - 100\text{h}^{-1}$, are associated with young seas and breaking across the entire wave spectrum, and the energy dissipation rates show up to $\pm 100\%$ variability about the mean for similar breaking rates. The majority of the HI data follow the same trend as the SBC data for infrequent breaking, but at much higher breaking rates, $R > 70\text{h}^{-1}$. At higher breaking rates $R > 100\text{h}^{-1}$ the relation between breaking rate and energy dissipation rate becomes more scattered, with $\pm 20\%$ variability about the mean.

[29] The slope of the $\Lambda(c_b)$ distribution is a direct measure of the relative contribution of different wave scales to the kinematics of wave breaking, such as the overturning of the air-sea interface. Phillips' model [*Phillips*, 1985] predicts a $\Lambda(c) \propto c^m$ dependence, where $m = -6$ within the equilibrium range, i.e., for $c_b \leq 0.7c_p$. Here we calculate the exponent $m$ of each $\Lambda(c_b)$ distribution by a best power-law fit within the range $c_1 < c_b \leq c_2$, where the lower bound $c_1$ is the speed associated with the peak of $\Lambda(c_b)$ and the upper bound is the largest resolved speed, or $c_2 = 8\text{ms}^{-1}$, whichever is less (see Figure 3).

[30] The slopes of the distributions (on a logarithmic scale), i.e., the fitted power law exponents, span a very

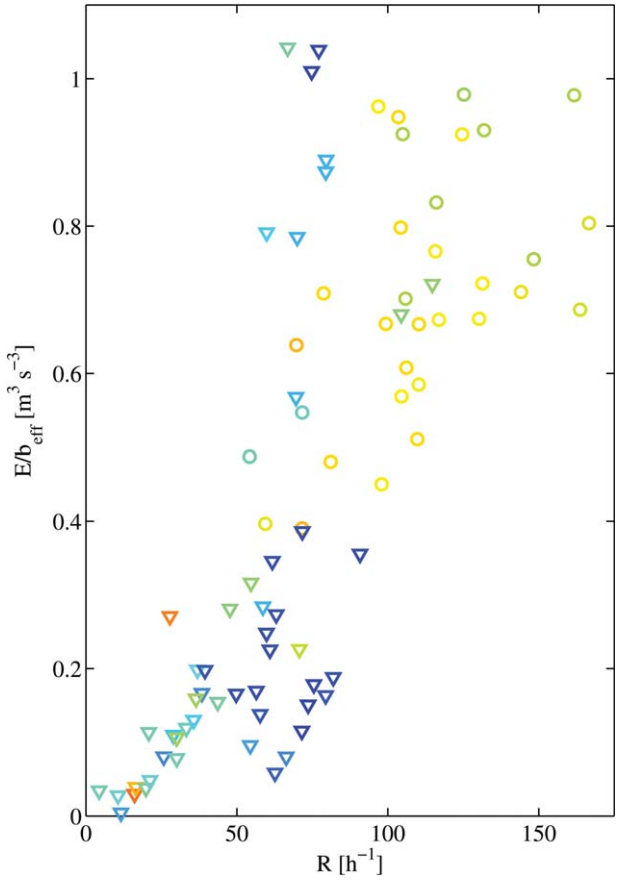


**Figure 8.** Scaled energy dissipation rate, $E/b_{\text{eff}} = \rho g^{-1} \int c_b^5 \Lambda(c_b) \mathrm{d}c_b$, as a function of the breaking rate $R$ for the Santa Barbara channel (triangles) and Hawaii experiment (circles). Colour coding depicts wave age (same scale as in Figure 3).

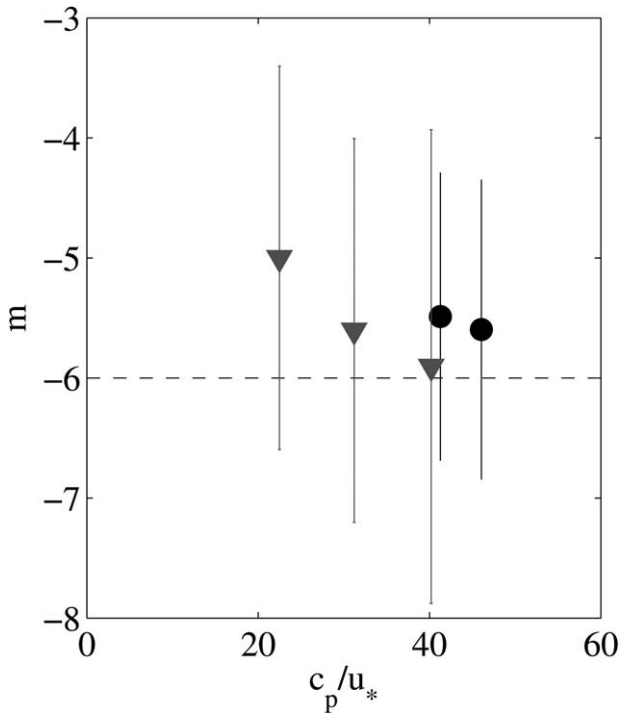


**Figure 9.** Bin-averaged exponent $m$ of the breaking crest length distribution as function of wave age for the Santa Barbara channel (gray triangles) and Hawaii experiment (black circles). The dashed line depicts the classical *Phillips* [1985] result $m = -6$. The vertical bars indicate $\pm 1$ standard deviation.

wide range: $-9.7 \leq m \leq -2.4$ for the Santa Barbara Channel experiment, and a slightly narrower range $-8.1 \leq m \leq -3.4$ during the Hawaii experiment. However, on average the exponent is $m > -6$ at a 90% significance level for both experiments. There is a general trend of decreasing $m$ values for increasing wave age (Figure 9). This trend is statistically significant at a 95% level, implying that larger-scale breakers become less frequent, and therefore less relevant to air-sea exchange processes, in older seas compared to younger seas. Only for the most developed seas in SBC ($c_p/u_* \approx 40$) is the average exponent of the distribution similar to the canonical value $m = -6$ (Figure 9).

[31] The rate of breaking in a given sea state is a function of the normalized wave saturation that is given by

$$\sigma(\omega) = 2g^{-2}\omega^5 S(\omega)/D(\omega), \tag{10}$$

where $D(\omega)$ is the directional spreading of the wave height spectrum $S(\omega)$ [*Banner et al.*, 2002; *Gemmrich et al.*, 2008].

[32] The spectral steepness of the wave field can be characterized by the weighted, band-averaged saturation

$$\sigma_b = \int_{\omega_p}^{4\omega_p} \omega^{-1}\sigma(\omega)\mathrm{d}\omega, \tag{11}$$

and the total energy dissipation rate due to wave breaking has been shown to be a function of $\sigma_b$ [*Gemmrich*, 2010]. Thus, it is likely that the exponent of the $\Lambda$ distribution depends on mean saturation as well. There is some indication in our data (at a 70% significance level) that the distributions have a lower exponent for increasing saturation, i.e., increasing breaking frequency (Figure 10). The spectrally resolved saturation $\sigma(\omega)$ is an increasing function of frequency for $\omega > \omega_p$ [*Banner et al.*, 2002; *Gemmrich et al.*, 2008]. Thus, at low overall saturation levels, only the highest frequencies surpass the threshold saturation level for the onset of breaking. With increasing saturation levels, this cutoff frequency moves toward lower frequencies and longer wave scales will break as well. This is consistent with the observed increase in $m$.

[33] Thus, the exponent of the breaking crest length distributions depends on the underlying wave field development, and individual data sets can be evaluated via wave age or wave saturation. However, we find a consistent offset between the SBC and HI data sets. Distributions from the central Pacific have lower exponents and are confined to shorter wave lengths. We remark that our data sets cover only a limited range of wave developments, and it would be desirable to have further observational confirmation of these dependences.

[34] As mentioned above, the breaking strength parameter $b_{\mathrm{eff}}$ relates the fifth moment of $\Lambda(c_b)$ to the energy dissipation rate (equation (6)). Hence, if an independent measure of the dissipation rate $E_{dis}$ is available, the effective breaking strength parameter may be estimated from $b_{\mathrm{eff}} = E_{dis}/\left(\rho g^{-1}\int c_b^5 \Lambda(c_b)\mathrm{d}c_b\right)$. *Gemmrich et al.* [2008] estimated $E_{dis} = c_{\mathrm{eff}}\,\tau$ from the energy input into the wave

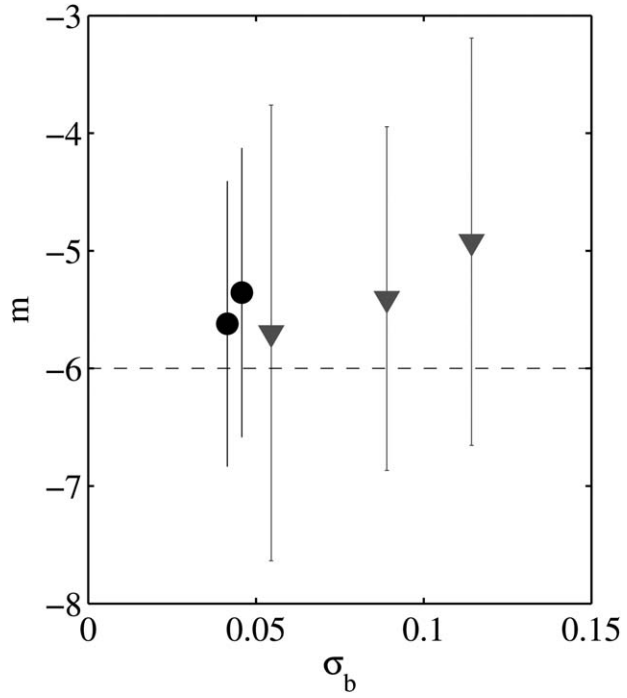


**Figure 10.** Bin-averaged exponent $m$ of the breaking crest length distribution as function of mean wave saturation $\sigma_b$ for the Santa Barbara channel (gray triangles) and Hawaii experiment (black circles). The dashed line depicts the classical *Phillips* [1985] result $m = -6$. The vertical bars indicate $\pm 1$ standard deviation.

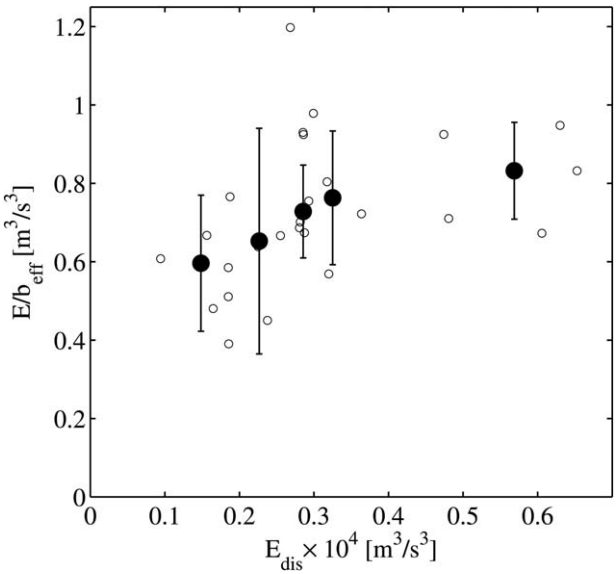


**Figure 11.** Scaled energy dissipation rate (integrated fifth moment of breaking crest length distributions, $E/b_{\mathrm{eff}} = \rho g^{-1} \int c_b^5 \Lambda(c_b) \mathrm{d}c_b$) as a function of the observed dissipation rate in the top 1.5 m of the water column, obtained from in situ velocity measurements for the Hawaii experiment. Open circles: estimates based individual 20 min data segments. Black dots: bin-averaged data, where the vertical bars indicate $\pm 1$ standard deviation.

field [*Gemmrich et al*., 1994]. Here we use a more direct method based on in situ dissipation rate measurements, similar to the approach in *Thomson et al*. [2009] and M. Schwendeman et al. (Wave breaking dissipation in a fetch limited seas, submitted to *Journal of Physical Oceanography*, 2013). Dissipation rate estimates are available for most of the HI data period [*Vagle et al*., 2012], but not for SBC. At intermediate turbulence levels the fifth moment scales linearly with dissipation rate (Figure 11), supporting the use of a scale-independent breaking strength parameter. At the highest dissipation levels observed, the increase of the fifth moment is less steep, which could indicate an increase in $b_{\mathrm{eff}}$ ; however, there are too few data points at very low and at high turbulence levels to determine a conclusive functional dependence of the fifth moment, and thus of $b_{\mathrm{eff}}$ , on turbulence levels. For the limited range of wave ages observed at HI, the resulting value of the effective breaking strength parameter is $b_{\mathrm{eff}} = 4.2 \times 10^{-5} \pm 1.8 \times 10^{-5}$ (Figure 12).

## 8. Conclusions

[35] While the applicability of Phillips' concept of breaking crest length distributions to the estimation of wave energy dissipation still requires a deeper understanding of the breaking strength parameter, it is clear that the breaking crest length distributions are a valuable tool for the assessment of air-sea exchange processes associated with wave breaking. There is also increasing interest to add breaking wave predictions to operational wave forecast model products. Results such as those presented here are critical for validating such breaking wave spectral model predictions [*Banner and Morison*, 2010] before these products can be issued as part of forecast alerts.

[36] Previous studies reporting breaking crest length distributions and breaking strength parameters were based on a variety of fundamentally different analysis methods and definitions of breaking speed and crest length. In particular, these inconsistent definitions are a significant cause for the widely scattered results in the shape and level of the breaking crest length distributions and the magnitude of the breaking strength parameter. Here we discuss two data sets which include a range of environmental conditions and breaking crest length distributions processed in a manner consistent with *Phillips* [1985] original conceptual framework.

[37] We directly measured the effective breaking strength parameter to be $4.2(\pm 1.8) \times 10^{-5}$ in mature seas with wave age $40 \leq c_p/u_* \leq 47$. We also found that the velocity scale of the breaking dissipation rate peak decreases with increasing wave age. Further, the breaking crest length

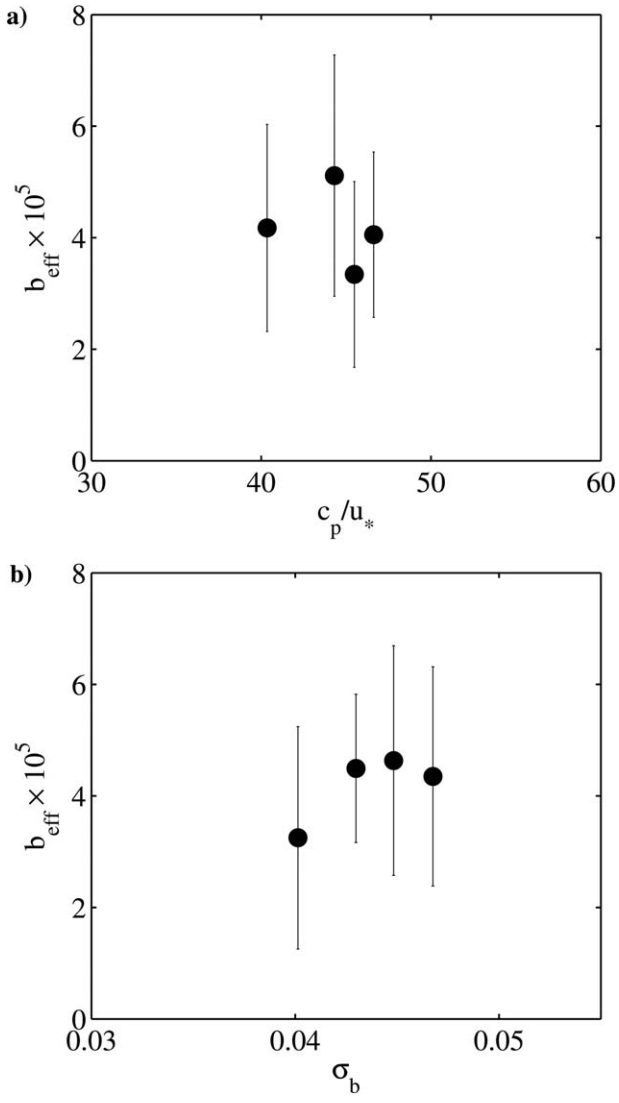


**Figure 12.** Bin-averaged effective breaking strength parameter $b_{\mathrm{eff}}$ for the Hawaii experiment as function of (a) wave age $c_p/u_*$ and (b) mean wave saturation $\sigma_b$.

spectrum falls off slower than the $c^{-6}$ behavior predicted by *Phillips* [1985]. This suggests that the breaking dominant waves in young seas exert a significant influence on the shape of $\Lambda$ and its moments. The integrated dissipation was significantly larger for mature seas compared to developing seas due to consistently higher energy and momentum fluxes from the wind. Further observational studies are needed to expand these simultaneous measurements of wave breaking geometry and turbulence within breakers for a wide dynamic range of sea states.

[38] **Acknowledgments.** We thank the captain and crews of R/P *FLIP* for their invaluable assistance during our field operations, and Svein Vagle (DFO Canada - IOS) for providing the raw Dopbeam data his group collected during the HI experiment. This work was funded by the Office of Naval Research under the Radiance Dynamics of the Ocean (RaDyO) DRI, with grants N00014-07-1-0015 (J. Gemmrich), N00014-06-1-0372 and N00014-11-1-0168 (C. Zappa), N00014-06-1-0047 and N00014-11-1-0054 (M.L.B. and R.P.M.). Comments by two anonymous reviewers helped us to improve the clarity of the paper.

## References

Babanin, A. (2011), *Breaking and Dissipation of Ocean Surface Waves*, Cambridge Univ. Press, Cambridge, U. K.

Banner, M. L., and R. P. Morison (2010), Refined source terms in wind wave models with explicit wave breaking prediction. Part I: Model framework and validation against field data, *Ocean Modell.*, *33*, 177–189.

Banner, M. L., J. R. Gemmrich, and D. M. Farmer (2002), Multiscale measurements of ocean wave breaking probability, *J. Phys. Oceanogr.*, *32*(12), 3364–3375.

Dickey, D. A., G. W. Kattawar, and K. J. Voss (2011), Shedding new light on light in the ocean, *Phys. Today*, *64*, 44–49.

Dickey, T., et al. (2012), Recent advances in the study of optical variability in the near-surface and upper ocean, *J. Geophys. Res.*, *117*, C00H20, doi:10.1029/2012JC007964.

Ding, L., and D. M. Farmer (1994), Observations of breaking surface wave statistics, *J. Phys. Oceanogr.*, *24*, 1368–1387.

Gemmrich, J. (2010), Strong turbulence in the wave crest region, *J. Phys. Oceanogr.*, *40*(3), 583–595.

Gemmrich, J. R., T. D. Mudge, and V. D. Polonichko (1994), On the energy input from wind to surface waves, *J. Phys. Oceanogr.*, *24*(11), 2413–2417.

Gemmrich, J. R., M. L. Banner, and C. Garrett (2008), Spectrally resolved energy dissipation rate and momentum flux of breaking waves, *J. Phys. Oceanogr.*, *38*(6), 1296–1312.

Kleiss, J., and W. K. Melville (2011), The analysis of sea surface imagery for whitecap kinematics, *J. Atmos. Oceanic Technol.*, *28*, 219–243.

Kleiss, J. M., and W. K. Melville (2010), Observations of wave breaking kinematics in fetch-limited seas, *J. Phys. Oceanogr.*, *40*, 2575–2604.

Massel, S. R. (2009), *Ocean Waves Breaking and Marine Aerosol Fluxes*, Springer, New York.

Melville, W. K., and P. Matusov (2002), Distribution of breaking waves at the ocean surface, *Nature*, *417*(6884), 58–63.

Mironov, A. S., and V. A. Dulov (2008), Detection of wave breaking using sea surface video records, *Meas. Sci. Technol.*, *19*, doi:10.1088/0957–0233/19/1/015405.

Perlin, M., W. Choi, and Z. Tian (2013), Breaking waves in deep and intermediate waters, *Annu. Rev. Fluid Mech.*, *45*, 115–145.

Phillips, O. M. (1985), Spectral and statistical properties of the equilibrium range in wind-generated gravity waves, *J. Fluid Mech.*, *156*, 505–531.

Phillips, O. M., F. L. Posner, and J. P. Hansen (2001), High range resoluiton radar measurements of the speed distribution of breaking events in wind-generated ocean waves: Surface impulse and wave energy dissipation rates, *J. Phys. Oceanogr.*, *31*(2), 450–460.

Rapp, R. J., and W. K. Melville (1990), Laboratory measurements of deep-water breaking waves, *Philos. Trans. R. Soc. London A*, *331*, 735–800.

Romero, L., W. Melville, and J. Kleiss (2012), Spectral energy dissipation due to surface wave breaking, *J. Phys. Oceanogr.*, *42*, 1421–1443.

Stansell, P., and C. MacFarlane (2002), Experimental investigation of wave breaking criteria based on wave phase speeds, *J. Phys. Oceanogr.*, *32*, 1269–1283.

Thomson, J., J. R. Gemmrich, and A. T. Jessup (2009), Energy dissipation and the spectral distribution of whitecaps, *Geophys. Res. Lett.*, *36*, L11601, doi:10.1029/2009GL038201.

Vagle, S., J. Gemmrich, and H. Czerski (2012), Reduced upper ocean turbulence and changes to bubble size distribution during large downward heat-flux events, *J. Geophys. Res.*, *117*, C00H16, doi:10.1029/2011JC007308.

Zappa, C. J., M. L. Banner, H. Schultz, J. R. Gemmrich, R. P. Morison, D. A. LeBel, and T. Dickey (2012), An overview of sea state conditions and air-sea fluxes during RaDyO, *J. Geophys. Res.*, *117*, C00H19, doi:10.1029/2011JC007336.